Author for correspondence:
Jakub Köry
e-mail: jakub.koery@glasgow.ac.uk

Discrete-to-continuum models of pre-stressed cytoskeletal filament networks

J. Köry, N. A. Hill, X. Y. Luo and
P. S. Stewart

School of Mathematics and Statistics, University of Glasgow, University Place, Glasgow G12 8QQ, UK

We introduce a mathematical model for the mechanical behaviour of the eukaryotic cell cytoskeleton. This discrete model involves a regular array of pre-stressed protein filaments that exhibit resistance to enthalpic stretching, joined at crosslinks to form a network. Assuming that the inter-crosslink distance is much shorter than the lengthscale of the cell, we upscale the discrete force balance to form a continuum system of governing equations and deduce the corresponding macroscopic stress tensor. We use these discrete and continuum models to analyse the imposed displacement of a bead placed in the domain, characterising the cell rheology through the force-displacement curve. We further derive an analytical approximation to the stress and strain fields in the limit of small bead radius, predicting the net force required to generate a given deformation and elucidating the dependency on the microscale properties of the filaments. We apply these models to networks of the intermediate filament vimentin and demonstrate good agreement between predictions of the discrete, continuum and analytical approaches. In particular, our model predicts that the network stiffness increases sublinearly with the filament pre-stress and scales logarithmically with the bead size.

THE ROYAL SOCIETY
PUBLISHING

1. Introduction

Eukaryotic cells exhibit a complicated rheology in response to mechanical stimuli, arising primarily through deformation of their cytoskeleton, a complex network of crosslinked filamentous proteins including actin filaments, microtubules and intermediate filaments (e.g. vimentin). In addition to stretching of the filaments themselves, the system also dissipates energy both through transport of viscous fluid through this network and through transient crosslink (CL) dynamics [1–3]. Depending on the rate at which the deformation is applied, cells have been shown to behave as visco-elastic, soft-glassy, or poro-elastic materials [4–7]. This complex rheology underpins a wide variety of cellular behaviour including migration and growth. In particular, epithelial cells can undergo an epithelial-mesenchymal transition, where these cells disassemble their cytoskeleton to become migratory [2]. Such transitions underpin healthy growth and development during embryogenesis and tissue repair [8,9], but also accompany progression of tumour cells towards more aggressive (i.e. invasive) phenotypes. Hence, a thorough knowledge of cell rheology (and in particular its mechanical properties) is a likely pre-requisite for successful anti-cancer treatments [2,10].

Tensegrity models of the cell cytoskeleton postulate that certain elements are pre-stretched which must be balanced by other elements under compression [11]. It is now well established that both actin and vimentin filaments *in vivo* are pre-stretched (i.e. under tension) [1,12]. On the other hand, microtubules have been shown to bear significant compressive loads [13,14] due to their large bending stiffness. Although actin and microtubules have generally attracted more attention in the literature, the intermediate filament vimentin also greatly impacts cell mechanics due to its capacity to withstand very large strains (especially in comparison with actin and microtubules) [15,16].

Most models describing the mechanical behaviour of individual cytoskeletal filaments have been derived using the theory of semi-flexible polymer chains [17], incorporating not only their elastic stretching and bending, but also uncoiling of their undulations under an applied stress [18]. As result, the distance between two ends of the filament differs from its stress-free contour length, so models relate the axial force applied to one end of the filament to the end-to-end distance normalized with respect to the contour length [17]. Similar relationships have also been derived based on the theory of Cosserat rods [19,20].

Due to the complexity of cell cytoplasm *in vivo*, *in silico* approaches are useful to elucidate the mechanisms underlying the mechanical behaviour on the network scale. Existing mathematical models typically fall into two categories. Discrete models of cell mechanics (including molecular dynamics simulations) enable the inclusion of detailed biophysics on the microscale derived from first principles, but also contain large number of discrete elements and their interactions which makes them computationally expensive [21–25]. On the other hand, continuum models of cell mechanics are typically much less computationally demanding, allowing fast parameter sweeps, but, because they are proposed to match macroscopic (i.e. cell-scale) phenomena, the manner in which microscale (molecular-scale) parameters and processes influence the macroscale response is often unclear [3].

The mechanical response of crosslinked networks of semiflexible filaments (e.g. actin or collagen) subject to various loading configurations has been studied using discrete network models elucidating key length and energy scales [26–29]. Under bulk deformations (uniaxial or shear strain), the dominant modes of deformation – material stretching, entropic stretching and bending – have been linked to the regions of affine and non-affine deformations in the parameter space consisting of the filament length and the crosslink density [26]. A similar approach has been subsequently used to mimic localized perturbations in cytoskeletal networks via point forces applied at a single crosslink [27]. Local deformations were further explored in recent years, modelling the stress stiffening of extracellular matrices induced by contractile cells pulling on the adjacent fibers [28,29]. However, at high filament densities encountered *in vivo*, the discrete simulations become computationally expensive [26] and as the networks are typically

highly disordered, there is no simple and reliable way to derive the corresponding continuum (computationally faster) model. Furthermore, scaling arguments do not account for the *in vivo* network pre-stress discussed above which makes direct utilization of the deduced power laws impossible.

The vast majority of macroscale continuum models are inferred by ensemble averaging based on polymer physics [17,30]. The models stemming from rubber elasticity form the oldest and largest group, including chain, full-network and microsphere models [31–35]. The latter have been applied to actin networks resulting in hyper-elastic and visco-elastic constitutive models [36–38]. Other approaches utilized Doi–Edwards theory [39] or the effective medium approach [40]. Discrete lattice models have also been employed, but to the best of our knowledge, rigorous upscaling techniques have not been used to derive a macroscale model. It is also worth noting that these discrete lattices often have unrealistic topologies - models using triangular lattices with coordination number 6 are not representative of crosslinked cytoskeletal networks and further care is needed to achieve a biologically realistic node connectivity [41,42]. Efforts involving more rational and rigorous mathematical methods (such as discrete-to-continuum upscaling or homogenization) to systematically bridge between these two approaches are still largely missing. This problem also pertains to collagen networks where predictions of discrete and continuum models often disagree [43,44].

Rational mathematical modelling has been successfully applied to study dynamic aspects of cytoskeletal reorganization during cell motility, including the dynamics of actin, myosin and other crosslinking proteins at the leading edge. This approach leads to mathematical formulations that are often amenable to analytical study and can provide explicit solutions, e.g. predicting the dependency of cell velocity on properties of the substrate [45,46]. However, such rational techniques have seldom been applied to study mechanics of crosslinked networks.

Recent research has focused on the effective transport properties of cytoplasm as a porous medium [47,48]; as a result, the forces generated within the cytoskeleton as it is deformed by the transported object remain incompletely understood. The force required to move a spherical object (bead) inside a living cell was recently measured using the optical tweezers, elucidating dependence on key parameters such as bead size and pulling velocity [7,15]. The primary goal of current study is to formalize these dependencies using a theoretical model built from first principles. To this end, we develop a multiscale framework for mechanical response during prescribed motion of an internal organelle or bead which rationally encodes a state-of-the-art microscale constitutive law for the axial stretching of individual semi-flexible filaments.

The paper is organized as follows. First, in Section 2 we introduce a discrete model of the cell cytoskeleton consisting of a two-dimensional crosslinked network with prescribed displacement of a set of CLs. In Section 3 we upscale this discrete force balance using discrete-to-continuum asymptotics, arrive at a macroscale continuum model equipped with appropriate boundary conditions and infer the corresponding stress tensor and strain-energy density. In Section 4 we compare simulations of the discrete and continuum models and numerically explore how net force exerted on the transported bead depends on key model parameters. In Section 5 we consider the limit of small deformations in the continuum problem and compute an asymptotic approximation to the net force as a function of bead displacement, valid whenever the bead size is much smaller than the macroscopic length scale.

2. Discrete model and nondimensionalization

(a) Initial network

(i) Geometry

We consider a planar square region within a eukaryotic cell of fixed side length $\tilde{D}$, well away from the nucleus and the cell membrane (Figure 1a). This region is parameterized by coordinates $\tilde{X}$ and $\tilde{Y}$, along the two edges of the square with origin at the centre. Focusing on mesh-forming

crosslinking proteins (e.g. filamin) we propose a simple model assuming that the cytoskeleton can be modelled as a square grid of semi-flexible filaments. Although this arrangement is highly idealized, it facilitates a formal upscaling. Moreover, the force-displacement curves arising from this square-grid arrangement are in strong quantitative agreement with an ensemble average of force-displacement curves computed from simulations of the same model applied to disordered networks of filaments; see Appendix A for further details. Initially the filaments are assumed to be equally spaced and are oriented (after averaging out microscale fluctuations) parallel to either the $\tilde{X}$ or $\tilde{Y}$ axes (blue lines in Figure 1a), with crosslinks (CLs) at their intersections, forming a regular two-dimensional grid. These CLs divide each filament into N filament segments (FSs). Initially these crosslinks are a distance $\tilde{R} = \tilde{D}/N$ apart, so crosslink (i,j) is located at

$$\tilde{\boldsymbol{X}}_{i,j} = \left(\tilde{X}_i, \tilde{Y}_j\right) = (i,j)\,\tilde{R}, \quad \text{where } i,j = -\tfrac{1}{2}N, -\tfrac{1}{2}N+1, ..., \tfrac{1}{2}N-1, \tfrac{1}{2}N; \tag{2.1}$$

we assume that N is even for simplicity. Note that throughout this work, tildes denote dimensional variables and parameters.
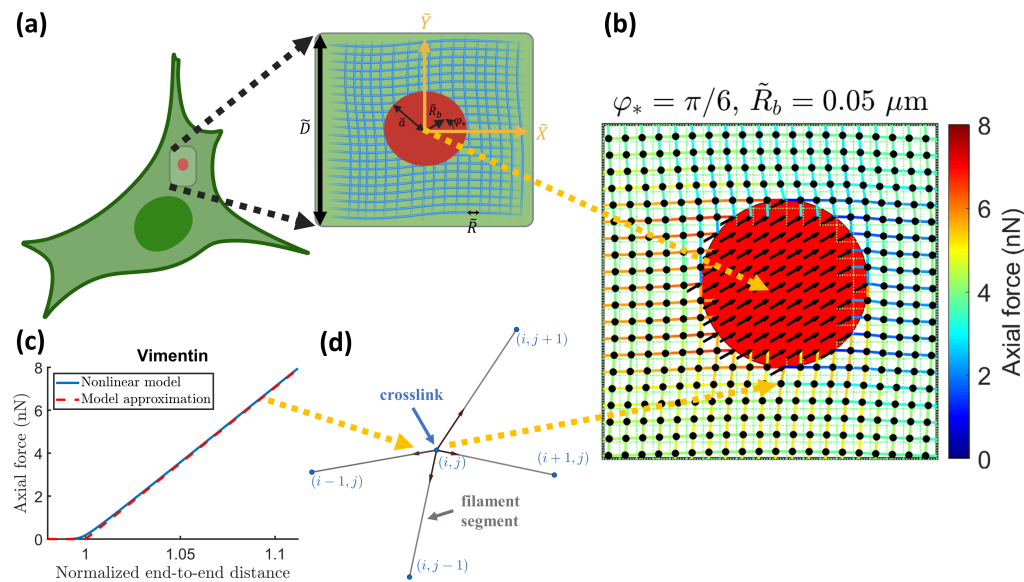

Figure 1: Panel (a) shows a cell schematic with a small inserted bead (red). Zooming onto the bead, we idealize the undeformed cytoskeleton as a regular grid of curved filaments (created with BioRender.com). Displacing the bead by a distance $\tilde{R}_b$ at an angle φ_*, we compute the locations of all crosslinks (black dots) in the perturbed network, as shown in panel (b). The calculation is based on a realistic microscale constitutive law for axial response of individual FSs (panel c) and assumes local force balance at CL (i,j) (panel d) with contributing forces drawn as black arrows. Panel (c) also documents that equation (2.9) provides an excellent approximation to model (2.3) for forces below tensile strength using default parameters for vimentin as estimated in Supplementary Section S2.

At subcellular scales, thermal effects play an important role causing undulations in cytoskeletal filaments even in the absence of external force. As result, a FS connecting arbitrary two neighbouring CLs need not be straight and its end-to-end distance need not be equal to its contour length (or arclength). For simplicity, we assume that all filaments are of the same stress-free contour length $\tilde{L}$, with the stress-free contour length of FSs being $\tilde{\Lambda} = \tilde{L}/N$, noting that these two quantities are typically distinct from the domain size $\tilde{D}$ and inter-CL distance $\tilde{R}$. Our model

contains a relatively large number of parameters; for convenience, our notation is summarized in Section S1 of Supplementary Material.

(ii) Pre-stretch

In later sections, we specialize our modelling framework to actin and vimentin networks; tensegrity models of the cytoskeleton postulate that these elements are typically pre-stretched [11]. For a fixed $\tilde{R}$, the filament pre-stretch is controlled by the normalized end-to-end distance

$$\xi = \frac{\tilde{R}}{\tilde{\Lambda}} = \frac{\tilde{D}}{\tilde{L}}, \tag{2.2}$$

which generates an axial force due to pre-stress denoted $\tilde{f}_p$. Although the macroscale pre-stress has been measured experimentally [13,49,50], the complexity of cytoskeleton *in vivo* (the number of different filaments and crosslinks and their interactions) makes it difficult to estimate $\tilde{f}_p$ and so this will be considered a free parameter (similar to previous studies, e.g. [51]). The corresponding values of $\tilde{\Lambda}$ and ξ then follow from the microscale constitutive law for the axial force discussed in the next section.

In experiments, the macroscale pre-stress is usually estimated by measuring the total force exerted on a particular surface within the cell, and then normalizing by the cross-sectional area of that surface [13]. Applying an analogous method to the boundary of our square domain, we estimate the macroscale pre-stress of our filament networks by summing the force exerted by each of the adjoining filaments on that boundary and dividing by the boundary length. In this way, we estimate the total macroscale pre-stress as

$$\tilde{\sigma}_p = \frac{(N-1)\tilde{f}_p}{\tilde{D}}.$$

(b) Deformed network

(i) Applied deformation

As a model for optical tweezers experiments [7,15], we consider the motion of circular bead of radius $\tilde{a}$ initially placed at the origin of the domain (Figure 1b). In this paper we restrict attention to quasi-static deformations, neglecting inertia and assuming zero net force on every CL for all time. In this simple model, we assume that CLs are free to rotate with no unfolding, unbinding, breakage or slippage. Thus, the energy supplied by the prescribed motion of the bead is stored as elastic energy in the filament network. The deformed coordinates of CL (i,j) are denoted as $\tilde{\boldsymbol{x}}_{i,j} = (\tilde{x}_{i,j}, \tilde{y}_{i,j})$.

(ii) Implicit microscale constitutive law for axial force in a filament segment

We denote $\tilde{r}$ as the distance between CLs after deformation. In this study we follow models for semi-flexible filaments, and let the axial force $\tilde{f}$ in each FS be a function of the end-to-end (straight-line) distance between its two end points normalized by its stress-free contour length $r = \tilde{r}/\tilde{\Lambda}$ (Figure 1c) [17,20]. Thus, tortuosity of individual FSs is accounted for implicitly. We use a well-established constitutive law for a single semi-flexible filament under tension, which includes the interplay between thermal undulations, bending stiffness and material extensibility [17,52], in the form

$$\frac{\tilde{r}}{\tilde{\Lambda}} = r(\tilde{f}; \tilde{\Lambda}) = \left(1 + \frac{\tilde{f}}{\pi \tilde{Y} \tilde{b}^2}\right)\left(1 - \sqrt{\frac{\tilde{k}_B \tilde{T}}{\pi \tilde{\Lambda}_p \left(\tilde{f} + \left(\pi^2 \tilde{k}_B \tilde{T} \tilde{\Lambda}_p / \tilde{\Lambda}^2\right)\right)}}\right), \tag{2.3}$$

where $\pi^2 \tilde{k}_B \tilde{T} \tilde{\Lambda}_p / \tilde{\Lambda}^2$ is the Euler buckling threshold force, $\tilde{k}_B \approx 1.38 \times 10^{-23} \mathrm{m}^2 \mathrm{kg}\,\mathrm{s}^{-2}\mathrm{K}^{-1}$ is the Boltzmann constant, $\tilde{T} = 300$ K is the absolute temperature, $\tilde{Y}$ is the Young's modulus, $\tilde{\Lambda}_p$ is the persistence length and $\tilde{b}$ is the radius of the filament under consideration. The constitutive law

(2.3) for an individual filament assumes that the stress-free contour length $\tilde{\Lambda}$ and the end-to-end distance $\tilde{r}$ are comparable (i.e. the normalized end-to-end distance r is close to 1, [18]). The first factor in (2.3) accounts for extensibility of the material while the second factor constitutes a model for an inextensible filament balancing thermal effects with its bending stiffness. Fixing all material parameters and substituting the initial values for $\tilde{r} = \tilde{R}$ and $\tilde{f} = \tilde{f}_p$ provides an implicit relationship between $\tilde{f}_p$ and $\tilde{\Lambda}$. Note that for extensible filaments, direct inversion to obtain $\tilde{f}$ as a function of r is cumbersome [17,20]. For a detailed description of the energy stored in individual FSs, see Supplementary Section S3.1.

(c) Force balance at a crosslink

The local force balance at each CL requires that the net force (Figure 1d) must be zero [53,54]. As the forces equilibrate at every CL, it follows that the total moment of forces about any CL is also zero. Note that apart from the axial forces, one would typically also need to introduce restoring forces due to the resistance of filaments to bending [54]. However due to the combination of high filament density and the imposed pre-stretch of actin and vimentin in our model, the response will be dominated by the elastic stretching and the bending can be neglected [18,26,41,55].

(d) Boundary conditions

All CLs on the outer boundary of the domain are assumed to be pinned, mimicking attachment to the membrane, nucleus or some other organelle. The bead is assumed to be at least as large as the mesh size (typically much larger, in line with the optical tweezers experiments [7]) and therefore a hole of appropriate shape and size must be extracted from the discrete network. To mimic a rigid body translation, we model the bead motion via an imposed displacement of all CLs within the initial outline of the bead by a distance $\tilde{R}_b$ at a pulling angle φ_* measured anti-clockwise from the $\tilde{X}$ axis.

(e) Baseline parameter values

We identify baseline parameter values representative of the cytoskeleton and denote these with the subscript c. For instance, we choose a baseline filament spacing as $\tilde{R}_c = 0.05\,\mu$m which, fixing the domain size as $\tilde{D} = 5\,\mu$m, means that every filament is divided into $N_c = 100$ FSs [7]. All other model parameters are listed and the corresponding values representative of the cytoskeleton are estimated in Supplementary Material (Section S2).

To ensure consistency as we vary the number of filaments, in simulations we hold the domain size and the total volume of filaments fixed to the baseline values by adjusting the mesh spacing and the filament radius according to

$$\tilde{R} = \frac{N_c}{N}\tilde{R}_c, \qquad \tilde{b} = \sqrt{\frac{N_c}{N}}\tilde{b}_c.$$

Similarly, we hold the macroscale pre-stress fixed by adjusting the filament pre-stress and analogously rescale the axial force at arbitrary r according to

$$\tilde{f}_p = \frac{N_c}{N}\tilde{\mathcal{F}}_p, \qquad \tilde{f}(r) = \frac{N_c}{N}\tilde{\mathcal{F}}(r),$$

where $\tilde{\mathcal{F}}(\xi) = \tilde{\mathcal{F}}_p$.

(f) Nondimensionalization

We nondimensionalize all lengths based on the domain side length $\tilde{D}$, and forces (including $\tilde{\mathcal{F}}_p$) with respect to the enthalpic (elastic) force $\pi\tilde{Y}\tilde{b}_c^2$. We denote as $l_{i\pm1/2,j}$ and $l_{i,j\pm1/2}$ the deformed

lengths of FSs connecting CL (i, j) to CLs $(i \pm 1, j)$ and $(i, j \pm 1)$, respectively. At CL (i, j), we define unit vectors pointing in the directions of the four adjacent FSs as

$$\hat{\boldsymbol{r}}_{i\pm\frac{1}{2},j} = \frac{(x_{i\pm1,j} - x_{i,j}, y_{i\pm1,j} - y_{i,j})}{l_{i\pm\frac{1}{2},j}}, \qquad \hat{\boldsymbol{r}}_{i,j\pm\frac{1}{2}} = \frac{(x_{i,j\pm1} - x_{i,j}, y_{i,j\pm1} - y_{i,j})}{l_{i,j\pm\frac{1}{2}}},$$

and upon multiplying by $\varepsilon_c N$, where $\varepsilon_c = N_c^{-1}$, the dimensionless force balance takes the form

$$\mathbf{0} = \mathcal{F}\left(\xi N l_{i-\frac{1}{2},j}\right) \hat{\boldsymbol{r}}_{i-\frac{1}{2},j} + \mathcal{F}\left(\xi N l_{i+\frac{1}{2},j}\right) \hat{\boldsymbol{r}}_{i+\frac{1}{2},j} + \mathcal{F}\left(\xi N l_{i,j-\frac{1}{2}}\right) \hat{\boldsymbol{r}}_{i,j-\frac{1}{2}} + \mathcal{F}\left(\xi N l_{i,j+\frac{1}{2}}\right) \hat{\boldsymbol{r}}_{i,j+\frac{1}{2}}.$$
(2.4)

The dimensionless magnitude of the bead displacement is denoted as $R_b := \tilde{R}_b / \tilde{D}$.

(g) Analysis of dimensionless microscale constitutive law

The dimensionless constitutive law for an individual filament (2.3) becomes

$$r(\mathcal{F}; \mathcal{T}_1, \mathcal{T}_2, \xi, \varepsilon_c, N) = (1 + \mathcal{F}) \left(1 - \sqrt{\frac{\mathcal{T}_1}{\mathcal{F}/(\varepsilon_c N) + 4\pi^3 \left(\varepsilon_c \xi N \mathcal{T}_2\right)^2 \mathcal{T}_1}}\right),$$
(2.5)

where

$$\mathcal{T}_1 = \frac{\tilde{\mathcal{F}}_{\text{entropic}}}{\tilde{\mathcal{F}}_{\text{enthalpic}}} = \frac{\tilde{k}_B \tilde{T}}{\pi^2 \tilde{Y} \tilde{b}_c^2 \tilde{\Lambda}_p} \qquad \text{and} \qquad \mathcal{T}_2 = \frac{\tilde{\Lambda}_p}{2\tilde{R}_c}$$
(2.6)

are the dimensionless ratios of the entropic force ($\tilde{\mathcal{F}}_{\text{entropic}} = \tilde{k}_B \tilde{T}/(\pi \tilde{\Lambda}_p)$) to the enthalpic force ($\tilde{\mathcal{F}}_{\text{enthalpic}} = \pi \tilde{Y} \tilde{b}_c^2$) and one half of the ratio of the persistence length to the end-to-end distance, respectively[1]. Note that all dimensionless parameters featuring in (2.5) are independent of the force due to pre-stress $\mathcal{F}_p$ and N, with the exception of ξ. Given that $\mathcal{F}(\xi) = \mathcal{F}_p$, we obtain

$$\xi = \{1 + \mathcal{F}_p\} \left\{1 - (\varepsilon_c N)^{-1} \left(\mathcal{F}_p (\varepsilon_c N)^{-3} \mathcal{T}_1^{-1} + 4\pi^3 \mathcal{T}_2^2 \xi^2\right)^{-1/2}\right\},$$
(2.7)

which provides a quartic polynomial for pre-stretch ξ as function of $\mathcal{F}_p$, which cannot easily be inverted analytically. However, for vimentin filaments we compute $\mathcal{T}_1 \approx 1.9 \times 10^{-8}$ and $\mathcal{T}_2 \approx 10$ (based on parameters listed in Table S1 in Supplementary Material) and so provided $\varepsilon_c N = O(1)$ and $\mathcal{F}_p \gg \mathcal{T}_1$ (i.e. the force due to pre-stress is much greater than the entropic force; for $\varepsilon_c N \gg 1$ we do not need any additional conditions) we approximate

$$\xi = 1 + \mathcal{F}_p.$$
(2.8)

The approximation (2.8) is not sufficiently accurate for actin, since $\mathcal{T}_1 \approx 10^{-9}$ but $\mathcal{T}_2 \approx 170$ (i.e. the persistence length of actin is much larger than the representative cytoskeletal mesh size), and an expansion in powers of $\mathcal{T}_2^{-1}$ is required (see Supplementary Material, Section S3.3).

In the main text we focus attention on networks of vimentin filaments. We further consider networks of actin filaments in Supplementary Material (Section S3.4), although here the critical stretch for filament breakage is typically very low and so the networks quickly disassemble.

In summary, the dimensionless problem is governed by eight dimensionless parameters ($\mathcal{T}_1$, $\mathcal{T}_2$, $\mathcal{F}_p$, ε_c, N, R_b, φ_*, a) and the microscale constitutive law (2.5), where ξ is given by (2.8). Model parameters and their default values are listed in Supplementary Material Section S2.

(h) Negligible response to compression and simplified microscale constitutive law

Neither actin nor vimentin filaments can sustain large compressive stresses due to their low bending stiffness [17]. We therefore assume that the response to compression is negligible, similar

---

[1] The factor of $1/2$ was chosen in line with previous studies so that our $\mathcal{T}_2$ is a direct analogue of the so-called normalized filament stiffness [17]. Note further that the r introduced in (2.3) should be regarded as a distance normalized with respect to the stress-free contour length and even though without units, this quantity is distinct from the nondimensionalized end-to-end distance (with respect to the macroscale).

to previous studies for actin networks [36,38] (vimentin filaments have even lower bending stiffness). Given the weak response of filaments to compression and also the smallness of $\mathcal{T}_1$ discussed in the previous section, we can neglect the square root term in (2.5) and using (2.8) derive a simplified microscale constitutive law (2.5) in the form

$$
\mathcal{F} = \begin{cases} \mathcal{F}_p + (r - \xi) = r - 1, & \text{if } r > 1 \\ 0, & \text{if } r < 1, \end{cases} \tag{2.9}
$$

which is continuous at $r = 1$, i.e. when the filament is straightened out to its full contour length ($\tilde{r} = \tilde{\Lambda}$), as (2.8) holds. Note that in the case of vimentin, this linearized expression was not obtained via Taylor expansion of the full model (2.5) about $r = \xi$, but was instead derived rationally based on the smallness of $\mathcal{T}_1$; it is analogous to previous models studying mechanics of pre-stressed filament networks [51]. Equation (2.9) provides a very good approximation to (2.3) using parameters pertinent to the intermediate filament vimentin (Figure 1c) across all values of r. The model (2.9) will be used in the sections of this paper where we present discrete and continuum simulations for vimentin. Note that it is possible, in principle, to simulate networks where filaments are modelled using (2.3) in its full form, but numerical simulations take significantly longer due to its implicit form.

It should be noted that the discrete model described above does not directly capture the mechanical behaviour of a disordered cytoskeletal filament network. However, we show in Appendix A that our regular approach can reproduce the mean mechanical response averaged over a large number of realisations of disordered networks (provided one accounts for the mean segment length). Moreover, in our model the filament pre-stress is maintained via the outer boundary and is thus not self-equilibrated. Despite these limitations, the discrete model described above is a prototypical model for studying the mechanical deformation of filament networks, providing a direct link between the microscale parameters and the macroscale response via a continuum upscaling (Section 3) and yields an explicit analytical formula for the network stiffness when pulling a small bead (Section 5).

3. Upscaling and continuum model

(a) Upscaling the force balance

We now define a small parameter $\varepsilon \equiv N^{-1} \ll 1$, the (dimensionless) undeformed CL-to-CL distance. We upscale the discrete model (2.4) in the limit $\varepsilon \to 0$ to form a continuum model. We assume that there exist smooth functions $x(X, Y)$ and $y(X, Y)$ defined on the square domain $-\frac{1}{2} < X, Y < \frac{1}{2}$ such that for all i, j we have $g(X_i, Y_j) = g_{i,j}$ where g is either x or y. Assuming x, y and $\mathcal{F}$ are sufficiently smooth, we Taylor expand the discrete equations (2.4) (centering about (X_i, Y_j)) and rationally derive a continuum model [56]. Further details of the derivation can be found in Supplementary Material (Section S4.1). The first non-trivial balance in the momentum equations gives

$$
\left(\mathcal{F}\left(\xi \sqrt{x_X^2 + y_X^2} \right) \frac{(x_X, y_X)}{\sqrt{x_X^2 + y_X^2}} \right)_X + \left(\mathcal{F}\left(\xi \sqrt{x_Y^2 + y_Y^2} \right) \frac{(x_Y, y_Y)}{\sqrt{x_Y^2 + y_Y^2}} \right)_Y = \mathbf{0}, \tag{3.1}
$$

where subscripts denote partial derivatives. This system of two coupled nonlinear equations in the divergence form constitutes the upscaled problem. Notice that in the (continuum) $N \to \infty$ limit, the constitutive law (2.5) converges to $\mathcal{F} = r - 1$ which is identical to (2.9); the resulting equations under the linearized microscale constitutive law are deduced in Supplementary Section S4.2.

The momentum balance equations (3.1) are consistent with other classical results in continuum mechanics (see Supplementary Material, Section S4.3, for details). Since these equations are expressed in divergence form, we can define $F_{kl} = \partial x_k / \partial X_l$ to be the components of the

corresponding deformation gradient tensor and immediately deduce the nominal stress tensor in the form

$$
\tilde{S} = \frac{1}{\tilde{R}_c}
\begin{pmatrix}
\tilde{\mathcal{F}}\left(\xi\sqrt{F_{11}^2 + F_{21}^2}\right)\dfrac{F_{11}}{\sqrt{F_{11}^2 + F_{21}^2}} & \tilde{\mathcal{F}}\left(\xi\sqrt{F_{11}^2 + F_{21}^2}\right)\dfrac{F_{21}}{\sqrt{F_{11}^2 + F_{21}^2}} \\[3mm]
\tilde{\mathcal{F}}\left(\xi\sqrt{F_{12}^2 + F_{22}^2}\right)\dfrac{F_{12}}{\sqrt{F_{12}^2 + F_{22}^2}} & \tilde{\mathcal{F}}\left(\xi\sqrt{F_{12}^2 + F_{22}^2}\right)\dfrac{F_{22}}{\sqrt{F_{12}^2 + F_{22}^2}}
\end{pmatrix}.
\tag{3.2}
$$

This formulation is a special case (reflecting the particular geometry of the undeformed configuration) of the stress tensor derived for an arbitrary distribution of filament directions using the Doi–Edwards construction [39]. In the initial configuration, $\boldsymbol{F} = \boldsymbol{I}$ and therefore $\tilde{S} = \tilde{\mathcal{F}}_p/\tilde{R}_c\boldsymbol{I}$, consistent with our prediction of macroscale pre-stress in Section 2(a). Similarly, we conclude that the dimensional strain energy density in the deformed configuration is

$$
\tilde{W}(\boldsymbol{C}) = \frac{\tilde{\mathcal{E}}\left(\xi\sqrt{I_4(\boldsymbol{C})}\right) + \tilde{\mathcal{E}}\left(\xi\sqrt{I_6(\boldsymbol{C})}\right)}{\tilde{R}_c^2},
\tag{3.3}
$$

where $\tilde{\mathcal{E}}$ denotes the energy stored in elastic stretching of the filaments (see Supplementary Material, Section S3.1), $\boldsymbol{C}$ is the right Cauchy–Green deformation tensor and $\sqrt{I_4(\boldsymbol{C})}$ and $\sqrt{I_6(\boldsymbol{C})}$ represent local stretches in X and Y directions, reflecting the underlying square-grid geometry of the cytoskeleton with two preferred filament directions. Such anisotropic contributions to the strain energy are often proposed in phenomenological models for fiber-reinforced materials (e.g. [57]).

(b) Boundary conditions

The pinning of the outer layer of CLs in the discrete model gives in the continuum limit

$$
x(X,Y) = X, \quad y(X,Y) = Y
\tag{3.4}
$$

along all boundaries characterized by $X = \pm\frac{1}{2}$ or $Y = \pm\frac{1}{2}$. In the continuum model, the bead is represented by a disc of radius $\tilde{a}$ cut out from the domain, initially centred at $(\tilde{X}, \tilde{Y}) = (0,0)$ and displaced by $\tilde{R}_b$ at a pulling angle φ_*. Note that in the dimensionless setting, we must have $a = \tilde{a}/\tilde{D} = O(1)$. The bead boundary condition is written for $-\pi < \varphi \leq \pi$ as

$$
x(a\cos(\varphi), a\sin(\varphi)) = a\cos(\varphi) + R_b\cos(\varphi_*), \qquad y(a\cos(\varphi), a\sin(\varphi)) = a\sin(\varphi) + R_b\sin(\varphi_*).
\tag{3.5}
$$

4. Discrete and continuum simulations

To facilitate direct comparison between the discrete and continuum predictions, we return to the dimensional variables and introduce the continuum displacement fields

$$
\tilde{u}(\tilde{X}, \tilde{Y}) = \tilde{x}(\tilde{X}, \tilde{Y}) - \tilde{X} \qquad \tilde{v}(\tilde{X}, \tilde{Y}) = \tilde{y}(\tilde{X}, \tilde{Y}) - \tilde{Y},
\tag{4.1}
$$

as well as their discrete counterparts

$$
\tilde{u}_{i,j} = \tilde{x}_{i,j} - \tilde{X}_i \qquad \tilde{v}_{i,j} = \tilde{y}_{i,j} - \tilde{Y}_j
\tag{4.2}
$$

for all i and j. Unless stated otherwise, all lengths (including those indicated in colorbars) are given in microns and all forces in nanonewtons.

In quasi-static simulations of the discrete model (2.4), we use numerical continuation from the initial configuration to find steady-state solutions for a variety of bead displacements. In order to avoid pulling along the initial direction of one of the filaments or exactly along the diagonal, we choose a default pulling angle as $\varphi_* = \pi/6$. To avoid FSs crossing each other, we only displace the bead up to a maximal distance equal to the undeformed mesh size, i.e. $0 \leq \tilde{R}_b \leq \tilde{R}$. For every $\tilde{R}_b$, we solve for the locations of CLs outside the bead using `fsolve` toolbox in MATLAB (based

on Newton's method) and then calculate the resultant force acting on the bead by summing up tensile forces from all attached FSs.

The continuum problem (3.1) is solved in FEniCS using Newton solver and we employed Lagrange finite elements of degree 1 [58]. As the difference in the predicted force on the bead using default model parameters, maximum displacement and domain resolutions (the minimum number of elements across the square in both $\tilde{X}$ and $\tilde{Y}$ directions) equal to 200 and 400 was less than 0.3% of the value at 200, we conclude that the resolution 400 provides us with a sufficiently fine mesh giving trustworthy force estimates. We use this value as default from now onwards. In the continuum model, the net force acting on the bead is then found by numerically integrating the traction ($\tilde{\boldsymbol{S}}^T \boldsymbol{N}$ where $\boldsymbol{N}$ is the unit normal to the bead) over the bead boundary.

(a) Simulation with default parameters for vimentin

In order to assess the convergence of discrete simulations to the continuum as $N \to \infty$, in Figure 2 we plot the force-displacement graphs for various N, fixing all other parameters at their default value (including $\varepsilon_c = 1/100$). In each case the graph of the magnitude of the force as a function of bead displacement (termed the force-displacement curve) is almost perfectly linear because we restrict attention to (small) deformations up to a single mesh size. For every given displacement the discrete and continuum predictions of the force approach one another as N becomes large (Figure 2a) and the results are almost indistinguishable for $N = 1/R_c = 100$. Note that the convergence is not monotonic for small N, but this is an artifact caused by the relatively small number of FSs attached to the bead in such cases. In order to elucidate how the steady state force distribution changes with increasing bead displacement, in the insets of Figure 2(a) we show the accumulation of tension in the wake of the moving bead. The solution profiles for such dense network ($N = 100$) are not easy to visualize and throughout this work we will therefore zoom onto a small region in the vicinity of the bead where the perturbation is localized. The magnitude of the continuum displacement field $||(\tilde{u}, \tilde{v})||$ (Figure 2b) shows good agreement with its discrete counter-part (Figure 2c). Note that the near-perfect symmetries of these fields with respect to the $\tilde{X}$ and $\tilde{Y}$ axes can be explained by the smallness of the deformation: while the nonlinear system (S29) does not suggest any symmetry, the structure of the small-deformations limit (5.4)-(5.7) derived in Section 5 (together with the symmetries of the domain under consideration) indicate that both components of the displacement field must be even functions of $\tilde{X}$ ($\tilde{Y}$) for a fixed $\tilde{Y}$ ($\tilde{X}$). In summary, this figure shows that the discrete and continuum predictions are in excellent agreement with one another as the mesh spacing reduces.

(b) Effect of model parameters

In this section we explore dependency on model parameters, namely the pulling angle φ_* (Section 4(b)i) and the force due to pre-stress $\tilde{\mathcal{F}}_p$ (Section 4(b)ii).

(i) Pulling angle φ_*

In order to assess the anisotropy of the force-displacement curves induced by our assumption of a regular array of filaments, in Figure 3 we examine the dependency on the pulling angle across its entire range. Amongst both the discrete and continuum simulations, the force-displacement curves remain within 1% of one another for the full range of pulling angles (Figure 3a,b). Furthermore, this difference remains small across the entire range of bead sizes considered (data not shown), consistent with the predictions of the continuum model in the limit of small deformations (see Section 5 below). As before, we observe good agreement between the continuum and discrete model predictions. However, despite the force exerted on the bead being almost independent of the pulling angle, we note that the overall stress profile is qualitatively different for different pulling angles (Figure 3c-f): the more aligned the direction of movement is with the initial direction of the filament, the greater the increase (decrease) in tension in the wake
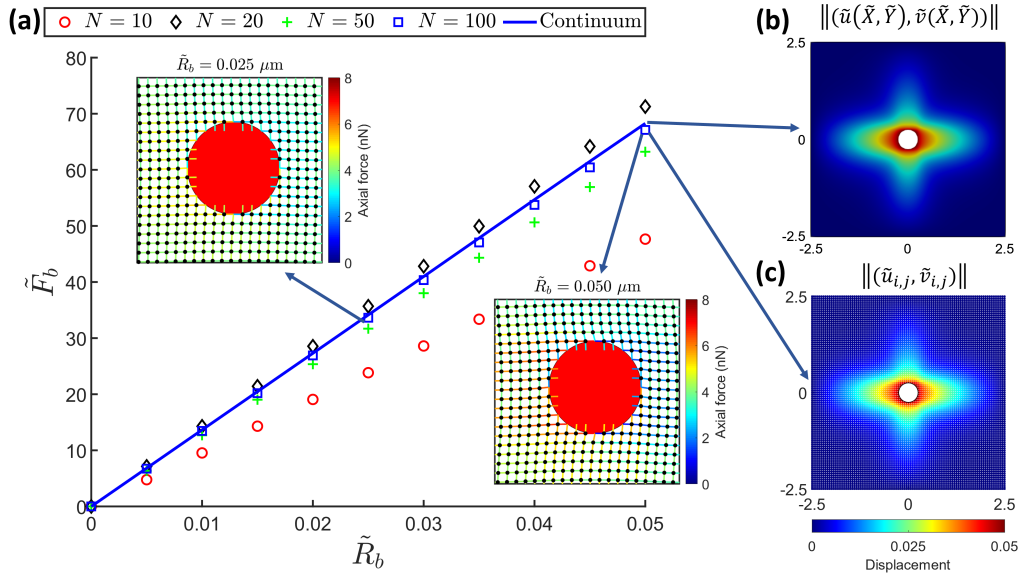
Figure 2: (a) The force-displacement graphs for increasing N in the discrete model (symbols) with default parameters converge to that for the continuum limit (solid blue). The insets depict solution profiles for $\tilde{R}_b = 0.025\mu$m and 0.05μm. Panels on the right show the magnitude of the displacement in the undeformed configuration in the continuum (b) and discrete (c) model (the latter visualized as a scatter plot).

(at the front) of the moving bead. In summary, this figure shows that while the force-displacement curve is approximately independent of the direction of bead movement, the stress profile within the material is sensitive to the direction of pulling.

(ii) Force due to pre-stress $\tilde{\mathcal{F}}_p$

In order to assess the importance of the filament pre-stress (since this is not known experimentally), in Figure 4(a) we study force response for increasing $\tilde{\mathcal{F}}_p$ and default parameters otherwise. As might be expected, with increasing (tensile) pre-stress in the filaments, the response gets stiffer, i.e. the gradient of the force-displacement curve increases. Due to the smallness of the deformations, the deviations from linear behaviour of the force-displacement curves are negligible in all studied cases which allows us to introduce a scalar measure of the network stiffness $\tilde{\mathcal{K}} = \mathrm{d}\tilde{F}_b/\mathrm{d}\tilde{R}_b$ which we approximate as $\max(\tilde{F}_b)/\max(\tilde{R}_b)$ evaluated at the largest bead displacement. The network stiffness increases with the pre-stress in a slightly sublinear manner (see the inset in Figure 4a). As expected, the overall force distribution within the network scales with the amount of pre-stress (Figure 4b,c).

5. Small-deformation and small-bead analysis

To provide further insight into the force-displacement relationship, and in particular the dependency on the model parameters, we investigate the limit $R_b \ll 1$, i.e. the limit of small macroscale deformations. Assuming that the bead displacement is small, it is natural to assume that all components of the deformation gradient tensor are small everywhere in the macroscopic domain. Note that the small deformations assumption is consistent with our restriction to bead displacements up to one inter-CL distance in the discrete model. We analyze small deformations by substituting

$$x(X,Y) = X + R_b\hat{x}(X,Y) + O(R_b^2), \qquad y(X,Y) = Y + R_b\hat{y}(X,Y) + O(R_b^2), \qquad (5.1)$$
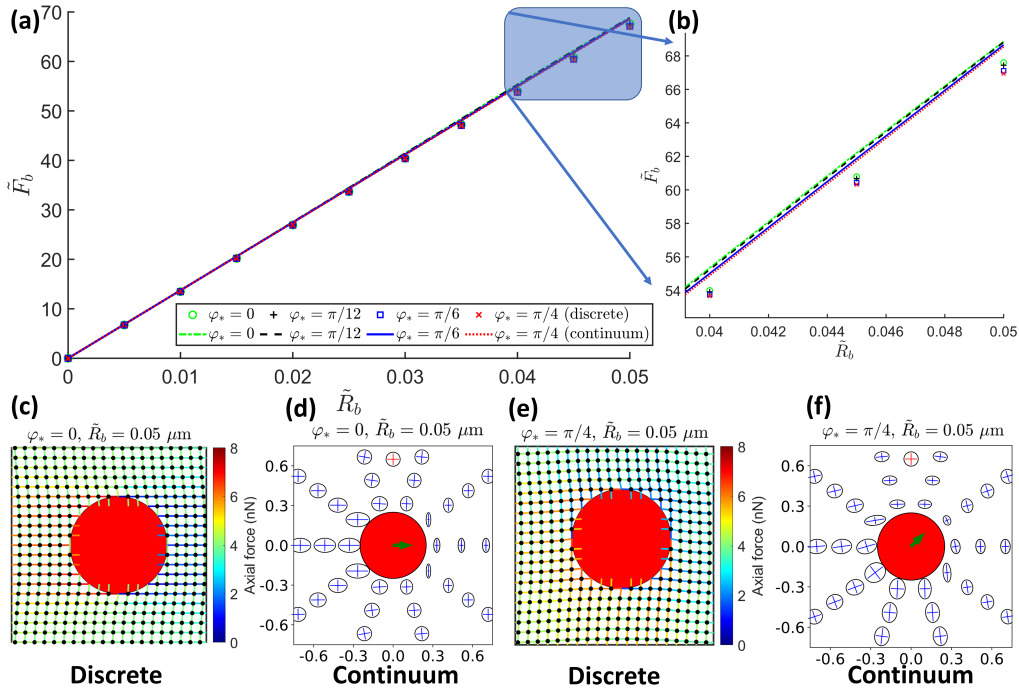
Figure 3: In panel (a), discrete (symbols) and continuum (lines) force-displacement graphs are plotted for default model parameters and for pulling angles 0 (green), $\pi/12$ (black), $\pi/6$ (blue) and $\pi/4$ (red) radians. As the resulting curves lie very close to one another for both models (and any fixed φ_*), to make the differences between various pulling angles visible, we zoom onto the maximum bead displacement in panel (b). Note that the force-displacement graphs for $\varphi_{**} \in (\pi/4, \pi/2)$ will mirror those for $\varphi_* = \pi/2 - \varphi_{**}$ due to the square shape of the macroscopic domain; in other words, due to the symmetry upon swapping X and Y. Panels (c) and (e) show the discrete solution profiles (zoomed-in onto the bead) at the largest displacement $\tilde{R}_b = \tilde{R} = 0.05\mu$m for two extreme values of the pulling angle $\varphi_* = 0$ (c) and $\pi/4$ (e) radians - the response is stiffest when one pulls in the direction of one of the two filament families and softest when pulling along the diagonal. The corresponding principal stresses and directions of the continuum stress tensor ($\boldsymbol{S}^T$) are plotted using ellipses at selected points near the bead in panels (d) and (f). Note that the continuum results are plotted using the undeformed variables with the corresponding pre-stress shown via red crossheads inside circles located at the top, that the green arrows indicate the direction of bead's motion and that the principal stresses were all normalized with respect to the same value chosen so that the ellipses do not overlap yet are large enough to be clearly seen.

with $R_b \ll 1$ into the continuum problem. Following Section S5.1 of the Supplementary Material, we arrive at the macroscale equations at $O(R_b)$

$$\left(\xi\mathcal{F}'(\xi)\hat{x}_X\right)_X + \left(\mathcal{F}(\xi)\hat{x}_Y\right)_Y = 0, \tag{5.2}$$

$$\left(\mathcal{F}(\xi)\hat{y}_X\right)_X + \left(\xi\mathcal{F}'(\xi)\hat{y}_Y\right)_Y = 0. \tag{5.3}$$

Note that equations (5.2) and (5.3) are decoupled. Since the constitutive law for the force in the FS is always monotonically increasing as a function of end-to-end distance (i.e. $\mathcal{F}'(\xi) > 0$), we can divide both equations by $\xi\mathcal{F}'(\xi)$ to obtain

$$\hat{x}_{XX} + \omega\hat{x}_{YY} = 0, \tag{5.4}$$

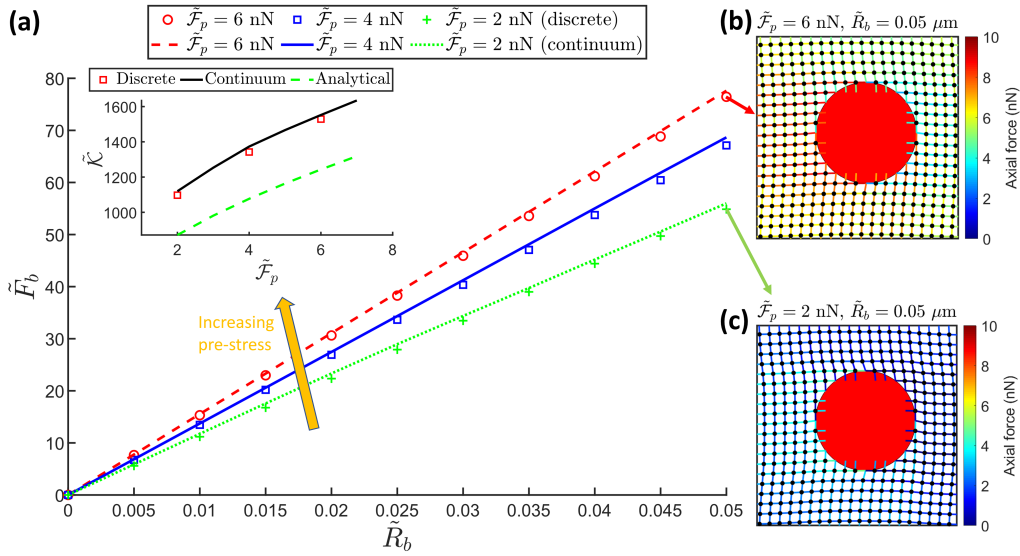$$\omega\hat{y}_{XX} + \hat{y}_{YY} = 0, \tag{5.5}$$

Figure 4: Force-displacement graphs for discrete (symbols) and continuum (lines) models for default model parameters and $\tilde{\mathcal{F}}_p = 2$ (green), 4 (blue) and 6 (red) nN (a). The inset shows the dependence of the effective stiffness $\tilde{\mathcal{K}} = \tilde{F}_b^{max}/\tilde{R}_b^{max}$ (evaluated at the maximum displacement) as function of $\tilde{\mathcal{F}}_p$. Panels on the right show solution profiles at $\tilde{R}_b = 0.05\mu$m for $\tilde{\mathcal{F}}_p = 6$ (b) and 2 nN (c).

where $\omega := \mathcal{F}(\xi)/(\xi\mathcal{F}'(\xi)) > 0$. For our particular FS constitutive law, $\mathcal{F} = r - 1$. These equations are subject to boundary conditions

$$\hat{x} = \hat{y} = 0, \tag{5.6}$$

evaluated on the outer boundary of the domain. Similarly, on the boundary of the bead (circle of radius a) we impose for any $-\pi < \varphi \leq \pi$ that

$$\hat{x}(a\cos(\varphi), a\sin(\varphi)) = \cos(\varphi_*), \qquad \hat{y}(a\cos(\varphi), a\sin(\varphi)) = \sin(\varphi_*). \tag{5.7}$$

For our choice of FS constitutive law we deduce $\omega = 1 - 1/\xi < 1$ which will be used in the elliptical transformation below (Figure 5). To the best of our knowledge it is not possible to solve (5.4)-(5.7) exactly. However, under the assumption $a \ll 1$, it is possible to find an asymptotic approximation valid in the inner region (i.e. close to $X^2 + Y^2 = a^2$). This assumption can easily be justified, as the beads used in optical tweezers experiments are typically small compared to the cell size [7].

(a) Solution in the limit $a \ll 1$

As the two equations are decoupled, we solve them separately. The technical details are presented in Supplementary Material (Section S5.2). The solution strategy for $\hat{x}$ ($\hat{y}$ problem is dealt with analogously) is summarized in Figure 5: we study the outer problem (5.4) subject to the outer boundary conditions together with the inner problem obtained by rescaling $(\bar{X}, \bar{Y}) = (X, Y)/a$, which localizes the problem to the neighbourhood of the bead (Figure 5a,b). In the inner region, we then need to transform the $\bar{Y}$ coordinate to $\bar{Z} = \bar{Y}/\sqrt{\omega}$ which transforms the governing equation into Laplace's equation on a (stretched) domain with an elliptical (inner) boundary (Figure 5c). Elliptical coordinates (S37) then allow us to transform this problem onto a semi-infinite strip while keeping the same governing equation so that an analytical solution can be found easily (Figure 5d). Undetermined constants in the inner solution are obtained by transforming back to Cartesian coordinates, writing in outer variables and matching with the
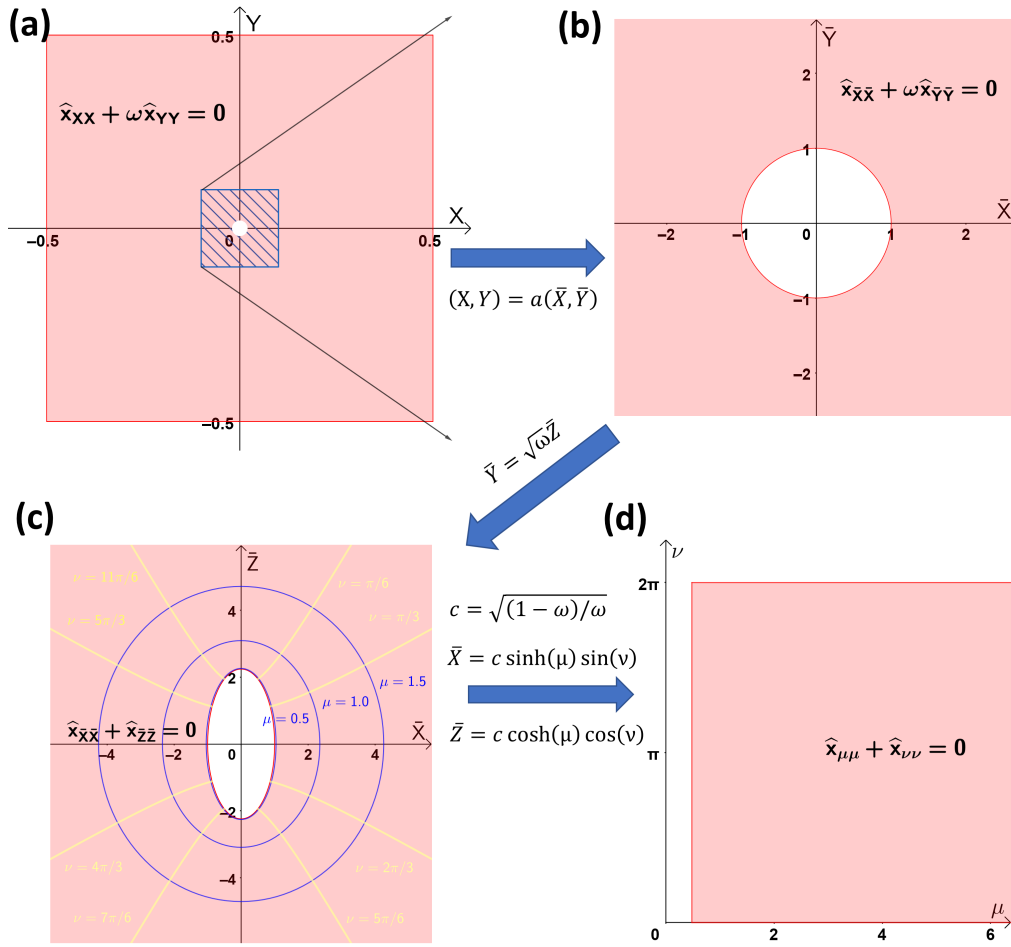
Figure 5: Demonstration of key steps in the solution process using $a = 0.02$ and $\omega = 0.2$. Starting from the macroscale variables (X, Y) (a) and assuming $a \ll 1$, we rescale to the inner layer (b). Then, we stretch the $\bar{Y}$ coordinate by the means of which we transform the governing equation into Laplace's equation which is to be solved subject to Dirichlet boundary conditions at an elliptical inner boundary in $(\bar{X}, \bar{Z})$ (c). Using elliptical coordinates - note in panel (c) that the blue curves correspond to $\mu = $ constant while yellow to $\nu = $ constant, the $\mu = \cosh^{-1}\left((1-\omega)^{-1/2}\right) \approx 0.5$ representing the inner boundary - we can finally transform this non-trivial geometry unto a rectangular one in (μ, ν) while keeping the governing equation same (d).

outer $\hat{x}$. Eventually, we conclude the inner approximation (denoted with superscript I)

$$\hat{x}^I = \cos(\varphi_*)\left\{1 + \frac{2\cosh^{-1}((1-\omega)^{-\frac{1}{2}}) - \ln\left(1 - 2q + 2\sqrt{q^2 - q}\right)}{2\ln(1/a) + \ln(4\omega/(1-\omega)) - 2\cosh^{-1}((1-\omega)^{-\frac{1}{2}})}\right\} + O\left(a^2\right), \quad (5.8)$$

where

$$q(\bar{X}, \bar{Y}) = \frac{-\omega\bar{X}^2 - \bar{Y}^2 + (1-\omega) - \sqrt{(\omega\bar{X}^2 + \bar{Y}^2 - (1-\omega))^2 + 4(1-\omega)\omega\bar{X}^2}}{2(1-\omega)}. \quad (5.9)$$

Similarly, to find an inner approximation for $\hat{y}$, we first transform $\bar{X}$ to $\bar{W} = \bar{X}/\sqrt{\omega}$ and then use elliptical coordinates (S44), where we derive

$$\hat{y}^I = \sin(\varphi_*) \left\{ 1 + \frac{2\cosh^{-1}((1-\omega)^{-\frac{1}{2}}) - \ln\left(1 - 2q_2 + 2\sqrt{q_2^2 - q_2}\right)}{2\ln(1/a) + \ln(4\omega/(1-\omega)) - 2\cosh^{-1}((1-\omega)^{-\frac{1}{2}})} \right\} + O\left(a^2\right), \quad (5.10)$$

where

$$q_2(\bar{X}, \bar{Y}) = \frac{-\bar{X}^2 - \omega\bar{Y}^2 + (1-\omega) - \sqrt{(\bar{X}^2 + \omega\bar{Y}^2 - (1-\omega))^2 + 4(1-\omega)\omega\bar{Y}^2}}{2(1-\omega)}. \quad (5.11)$$

Differentiating (5.8) and (5.10) with respect to X and Y we deduce leading-order approximations for the strain fields away from the bead (see Supplementary Material, Section S5.3).

(b) Stress field and net force exerted on the bead

Substituting the small-deformations ansatz (5.1) into the stress tensor (3.2) we further expand using $R_b \ll 1$ to obtain in the inner layer

$$\tilde{S} = \frac{\pi\tilde{Y}\tilde{b}_c^2}{\varepsilon_c\tilde{D}} \left\{ \begin{pmatrix} \mathcal{F}(\xi) & 0 \\ 0 & \mathcal{F}(\xi) \end{pmatrix} + R_b \begin{pmatrix} \xi\mathcal{F}'(\xi)\hat{x}_X^I & \mathcal{F}(\xi)\hat{y}_X^I \\ \mathcal{F}(\xi)\hat{x}_Y^I & \xi\mathcal{F}'(\xi)\hat{y}_Y^I \end{pmatrix} + O(R_b^2) \right\}. \quad (5.12)$$

As in the full continuum problem, the net force exerted on the bead is calculated by integrating $\tilde{S}^T N$ over the boundary of the bead $\bar{X}^2 + \bar{Y}^2 = 1$ using the displacement profiles (5.8) and (5.10) in the inner layer. Performing these calculations and using the constitutive law (2.9) (details are included in Supplementary Material, Section S5.4), we derive an analytical expression for the force response of the material to the bead being pulled through it valid asymptotically (accurate up to $O(a)$ error) of the form

$$\tilde{F}_b \approx -(\cos(\varphi_*), \sin(\varphi_*))\tilde{F}_b^0, \quad (5.13)$$

where

$$\tilde{F}_b^0 = \frac{2\pi R_b/\varepsilon_c\sqrt{\mathcal{F}_p(1 + \mathcal{F}_p)}}{\ln\left(2\left(\sqrt{\mathcal{F}_p(1 + \mathcal{F}_p)} - \mathcal{F}_p\right)/a\right)} \pi\tilde{Y}\tilde{b}_c^2. \quad (5.14)$$

Note that this force on the bead is in the direction opposite to that of the pulling, as expected. Equation (5.14) elucidates how the force-displacement curve depends on key model parameters, namely filament's pre-stress $\mathcal{F}_p$, Young's modulus $\tilde{Y}$ and radius $\tilde{b}_c$, mesh spacing ε_c and bead radius a. Finally, we deduce an analytical formula for the (dimensional) effective network stiffness

$$\tilde{\mathcal{K}} = \frac{d\tilde{F}_b}{d\tilde{R}_b} \approx \frac{\tilde{F}_b^0}{\tilde{R}_b} = \frac{\pi\tilde{Y}\tilde{b}_c^2}{\tilde{R}_c} \frac{2\pi\sqrt{\mathcal{F}_p(1 + \mathcal{F}_p)}}{\ln\left(2\left(\sqrt{\mathcal{F}_p(1 + \mathcal{F}_p)} - \mathcal{F}_p\right)/a\right)}. \quad (5.15)$$

Note from the inset in panel (a) of Figure 4 that for the default bead size, the analytical result is already in good qualitative agreement with the discrete and continuum models.

(c) Dependence of force response on the bead size

In order to assess the comparison between discrete, continuum and analytical approaches, in Figure 6(a) we plot force-displacement curves for a number of values of a. The discrete and continuum model results agree well for all considered values and, as expected, the larger the bead is the greater the force required for its transport. Moreover, as a decreases, our asymptotic result (5.14) approaches simulation results of the continuum model. More specifically, as a is reduced from 0.1 to 0.025, the absolute (relative) approximation error at the maximum displacement ($\tilde{R}_b = 0.05\mu$m) decreases from roughly 28 nN to 8 nN. Figure 6(b) confirms the increasing agreement between the direct numerical simulations of the continuum model and our analytical approximation as a is further reduced. When plotted using logarithmic scales on both axes, the

continuum model predictions do not collapse onto a straight line indicating that the net force does not scale with a according to a power law but behaves in the logarithmic manner instead (c.f. equation (5.14)). Note that the continuum and analytical results almost overlap for $a = 1/400$. The discrete solution profiles at the maximum displacement value $\tilde{R}_b = 0.05\mu m$ for varying bead radius a are presented in Figures 6(c,d,e). With decreasing a, the number of FSs exerting force on the bead decreases linearly, but their individual stretches (and hence forces) are larger. In summary, this figure confirms that discrete and continuum predictions converge to the analytical formula (5.14) thus establishing it as a useful predictor of the net force exerted on a small bead.
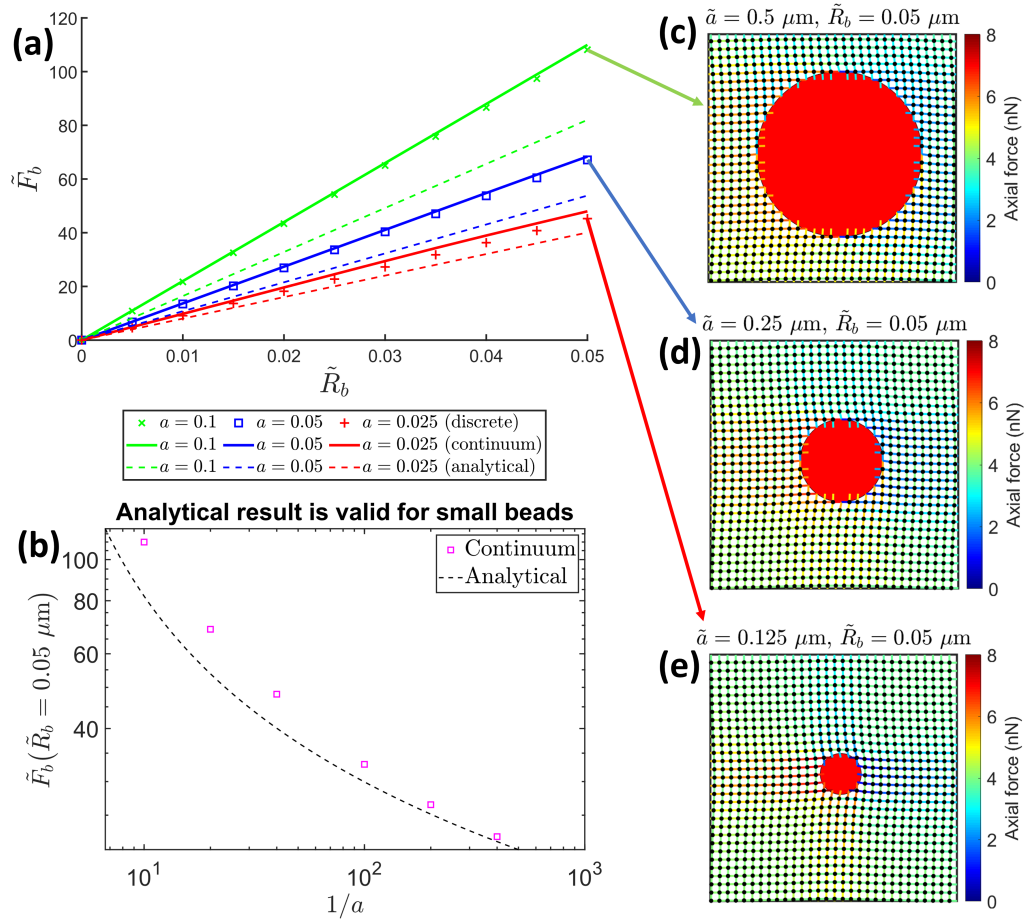

Figure 6: (a) Force-displacement curves for default model parameters and the bead radius equal to twice ($0.5\mu m$; green) and half ($0.125\mu m$; red) the default value ($0.25\mu m$; blue), with panels (c), (e) and (d) showing the corresponding solution profiles at the maximum displacement, $\tilde{R}_b = 0.05\mu m$. Panel (b) demonstrates the convergence of the continuum simulations onto the prediction of the $a \ll 1$ asymptotics.

6. Discussion

In this paper we have developed a multiscale framework for modelling the mechanical response of the eukaryotic cell cytoskeleton to internal motion of a small internal bead or organelle, mimicking recent rheological tests using optical tweezers [7]. In particular, we have developed a discrete model of the cell cytoskeleton by assuming a planar regular square grid of cytoskeletal

filaments, using a microscale constitutive law for the mechanical response of each filament segment (Figure 1) [17] . This model is highly idealized, ignoring the complex irregular geometry of the cytoskeletal network, including three-dimensional effects, and representing the structure by just one type of filament (in this case the intermediate filament vimentin). However, the simplicity of our framework allows a rational upscaling of the discrete model, from which we can construct a macroscale continuum model which encodes the microscale properties of the individual filaments. This continuum model provides an excellent match to discrete simulations across the parameter space at a fraction of the computational cost. Furthermore, in the limit of small bead displacements the continuum model can be solved asymptotically for small bead size by stretching the geometry of the (bead) boundary region, transforming to elliptical coordinates and matching with the outer region (Figure 5), from which it is possible to construct a closed form expression (5.14) for the net force acting on the bead as a function of its size, the Young's modulus and radius of the filaments, the angle at which the bead is pulled through the network relative to the filaments, the network pre-stress and its spacing. In future, expression (5.14) could in principle be used to infer an estimate of a microscale filament pre-stress from the macroscale force-displacement data. The option of having both discrete and continuum formulation allows us to consider a variety of sizes of transported objects. For example, cell organelles are often much larger than the mesh size so that the continuum description for cytoskeleton is justified and computationally inexpensive (and one can make use of our analytical result (5.14)). Conversely, the discrete simulations without a hole would form an appropriate model for transport of small cytoplasmic molecules which are usually smaller than the mesh spacing [7].

A unified picture emerges from solving these discrete, continuum and analytical models: the system predicts an approximately linear relationship between the force on the bead and its displacement, and the gradient of this curve provides an estimate of the network stiffness (Figure 2). In particular, we show that the anisotropy introduced by the square symmetry of our networks is present but weak so that the response is nearly isotropic, i.e. the network stiffness is approximately independent of the angle at which the bead is pulled through the structure (Figure 3), consistent with the optical tweezers experiments [7]. The net force F_b increases sublinearly with the filament pre-stress across the studied range although the deviation from linear behaviour is small (Figure 4) and decreases in a logarithmic manner ($F_b \propto (\ln (1/a) + \mathrm{const})^{-1}$) as the radius of the bead (a) reduces (Figure 6). We note that a linear increase in network stiffness with increasing pre-stress is found in tensegrity studies of cell mechanics, even though such linearity is typically established under bulk (shearing) deformations as opposed to local perturbations studied here [1].

Numerical simulations in the absence of pre-stress take significantly longer than their pre-stretched counterparts. Initially stress-free networks thus appear to be the borderline case beyond which (pre-compressed filaments) neither discrete (MATLAB) solver nor continuum (FEniCS) solver converge. By analogy with the literature on central force networks we therefore expect that the problem with initially stress-free network suffers from ill-posedness issues associated with the so-called stiffness percolation (positive elastic modulus at zero strain) [18]. In our model, the pre-stress is maintained by the outer boundary enforcing a total filament length greater than the natural length. Our modelling framework could potentially be generalized to include two or more cytoskeletal components (e.g. actin stress fibers, microtubules etc), where each component exhibits differing amounts of pre-stretch (or pre-compression), allowing the system to find an equilibrated state of pre-stress without enforced displacement at the boundaries. Furthermore, our analysis in this study is mostly restricted to quasi-static deformations of regularly arranged filament networks which remain in-tact as the deformation is applied. However, eukaryotic cells are known to exhibit a complicated rheology involving additional dissipative effects arising from motion of the filaments through the surrounding cytoplasmic fluid [6] and through transient crosslink binding/unbinding, sliding and unfolding [22,59–61]. We have recently extended the framework from this paper to include some of these additional features, modelling the cell as

a poro-visco-elastic continuum material, allowing exploration of how these different mechanical responses manifest in different cell types [62].

In this study we have primarily restricted to regularly arranged filament networks with fixed coordination number. However, the discrete framework presented in this paper can readily be extended to disordered filament networks and also to include filament breakage, allowing the possibility of localised non-affine deformations [43]. Indeed, preliminary simulations suggest that the predictions from the ordered network simulations presented in the main text are a useful indicator of the behaviour of a disordered filament network (see Appendix A); further consideration of disordered networks is deferred to future work.

The discrete-to-continuum modelling approach is not restricted to cytoskeletal networks and could similarly be applied to other crosslinked networks of semi-flexible filaments such as collagen [44]. Furthermore, our approach could be modified to model cells migrating through (and interacting with) extra-cellular matrix [25,63,64].

Appendix A. Application to disordered filament networks

In this appendix we apply the model constructed in Section 2 to disordered networks of filaments.

To generate a (random) disordered network we seed N_f constituent filaments as straight lines randomly spanning the square domain. We randomly fix the geometry of each filament by choosing a single point on the line (sampling both the x and y coordinates from a uniform distribution spanning the range of the square domain) and the gradient of the line (again sampling from a uniform distribution for the tangent of the angle to the X direction). We endow each filament with the same microscale constitutive law as the regular networks (the dimensionless equation (2.9), equivalent to the dimensional equation (S14)) and with the same pre-stress (see Section S2 of the Supplementary Material). As in the regular model we assume crosslinks are formed at each filament crossing and at each point where the filament crosses the outer boundary of the square domain.

In simulations presented here we fix the number of filaments as $N_f = 38$ (which corresponds to $N = 20$ for the regular array). Two representative examples of disordered networks are shown in Figure 7(a,b). Over 100 random realisations of the network structure this results in an average of approximately 481 crosslinks across the square domain (compared to 437 for the regular array) and an average filament segment length of $0.2142\,\mu$m (compared to $0.25\,\mu$m for the regular array).

To deform the network we displace the crosslink closest to the centre of the domain (displaced cross-link shown as red circle in Figure 7a,b), focusing attention on a single value of the pulling angle $\varphi_* = 0$; similar to the simulations in the main paper we consider small deformations up to $0.02\,\mu$m.

Applying this displacement protocol to 100 random realisations of the initial network, we calculate the mean and the standard deviation of the force-displacement curve (shown as the solid blue line in Figure 7c). The predicted force-displacement curve from the regular network for an equivalent number of filaments ($N = 20$) lies within one standard deviation of this mean (the dashed red line in Figure 7c). However, as discussed above the number of crosslinks and the

mean filament segment lengths are not directly comparable. Our analytical model from Section 5 indicates that the gradient of the force-displacement curve is inversely proportional to the initial filament segment length (see equation (5.15)). In this spirit, one approach to reconcile the two approaches is to rescale the force-displacement curve from simulations of the regular network by the ratio of the filament segment length from the ordered network to the mean filament segment length from the disordered networks; this rescaled force-displacement curve collapses almost perfectly onto the mean obtained for the disordered networks (the dotted black line in Figure 7c). Alternatively, we can increase the number of filaments in the ordered network to produce a filament segment length more comparable to that of the disordered networks. For example, for $N = 24$ in the ordered network the system exhibits a filament segment length of 0.2083 μm, and the corresponding force-displacement curve again shows much closer agreement with the mean from the simulations of the disordered networks (the dash-dotted green line in Figure 7c). These preliminary observations suggest that the predictions of the ordered network simulations presented in the main text are a useful indicator of the behaviour of a disordered filament network, with the significant advantage that the regular network can be formally upscaled into a continuum description.

References

1. Mofrad MR, Kamm RD. 2006 *Cytoskeletal mechanics: models and measurements in cell mechanics*. Cambridge University Press.
2. Alberts B. 2017 *Molecular biology of the cell*. WW Norton & Company.
3. Vaziri A, Gopinath A. 2008 Cell and biomolecular mechanics in silico. *Nat Mater* **7**, 15–23.
4. Sato M, Ohshima N, Nerem R. 1996 Viscoelastic properties of cultured porcine aortic endothelial cells exposed to shear stress. *J Biomech* **29**, 461–467.
5. Fabry B, Maksym GN, Butler JP, Glogauer M, Navajas D, Fredberg JJ. 2001 Scaling the microrheology of living cells. *Phys Rev Lett* **87**, 148102.
6. Moeendarbary E, Valon L, Fritzsche M, Harris AR, Moulding DA, Thrasher AJ, Stride E, Mahadevan L, Charras GT. 2013 The cytoplasm of living cells behaves as a poroelastic material. *Nat Mater* **12**, 253–261.
7. Hu J, Jafari S, Han Y, Grodzinsky AJ, Cai S, Guo M. 2017 Size-and speed-dependent mechanical behavior in living mammalian cytoplasm. *Proc Natl Acad Sci U S A* **114**, 9529–9534.
8. Ahmed WW, Betz T. 2015 Dynamic cross-links tune the solid–fluid behavior of living cells. *Proc Natl Acad Sci U S A* **112**, 6527–6528.
9. Serrano JC, Gupta SK, Kamm RD, Guo M. 2021 In pursuit of designing multicellular engineered living systems: A fluid mechanical perspective. *Annu Rev Fluid Mech* **53**, 411–437.
10. Thiery JP, Acloque H, Huang RY, Nieto MA. 2009 Epithelial-mesenchymal transitions in development and disease. *Cell* **139**, 871–890.
11. Ingber DE. 2003 Tensegrity I. Cell structure and hierarchical systems biology. *J Cell Sci* **116**, 1157–1173.
12. Charras GT, Horton MA. 2002 Single cell mechanotransduction and its modulation analyzed by atomic force microscope indentation. *Biophys J* **82**, 2970–2981.
13. Wang N, Naruse K, Stamenović D, Fredberg JJ, Mijailovich SM, Tolić-Nørrelykke IM, Polte T, Mannix R, Ingber DE. 2001 Mechanical behavior in living cells consistent with the tensegrity model. *Proc Natl Acad Sci U S A* **98**, 7765–7770.
14. Brangwynne CP, MacKintosh FC, Kumar S, Geisse NA, Talbot J, Mahadevan L, Parker KK, Ingber DE, Weitz DA. 2006 Microtubules can bear enhanced compressive loads in living cells because of lateral reinforcement. *J Cell Biol* **173**, 733–741.
15. Hu J, Li Y, Hao Y, Zheng T, Gupta SK, Parada GA, Wu H, Lin S, Wang S, Zhao X et al.. 2019 High stretchability, strength, and toughness of living cells enabled by hyperelastic vimentin intermediate filaments. *Proc Natl Acad Sci U S A* **116**, 17175–17180.
16. Patteson AE, Carroll RJ, Iwamoto DV, Janmey PA. 2020 The vimentin cytoskeleton: when polymer physics meets cell biology. *Phys Biol* **18**, 011001.
17. Meng F, Terentjev EM. 2017 Theory of semiflexible filaments and networks. *Polymers* **9**, 52.
18. Pritchard RH, Huang YYS, Terentjev EM. 2014 Mechanics of biological networks: from the cell cytoskeleton to connective tissue. *Soft matter* **10**, 1864–1884.
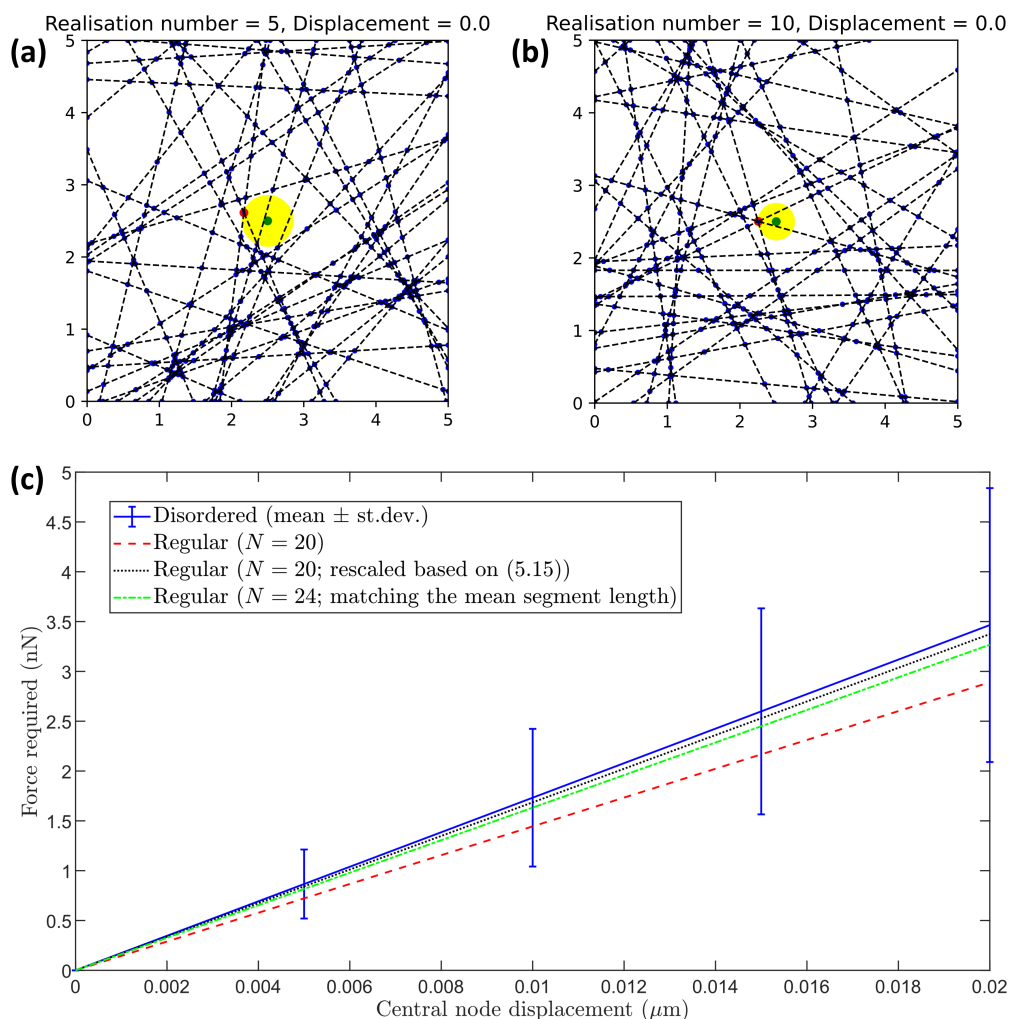
Figure 7: Panels (a) and (b) present two representative examples of disordered networks with 38 filaments (corresponding to $N = N_c = 20$) in their initial configuration. The filaments are plotted with dashed black lines, the crosslinks with blue circles, the centre of the domain is depicted with a green circle and the crosslink nearest to this point (which is to be transported in the X−direction) with a red circle. Panel (c) shows the mean and the standard deviation of the force response over 100 such randomly selected disordered networks (solid blue), the force response of the square-grid network (as studied in this manuscript) with the same number of filaments ($N = 20$; dashed red), the response rescaled based on equation (5.15) (dotted black) and the response of the square-grid network with N selected to (approximately) match the mean segment length in disordered networks ($N = 24$; dash-dotted green), as described in the main text.

19. Holzapfel GA, Ogden RW. 2011 On the bending and stretching elasticity of biopolymer filaments. *J Elast* **104**, 319–342.

20. Holzapfel GA, Ogden RW. 2013 Elasticity of biopolymer filaments. *Acta Biomater* **9**, 7320–7325.

21. Kim T, Hwang W, Kamm R. 2009 Computational analysis of a cross-linked actin-like network. *Exp Mech* **49**, 91–104.

22. Lee H, Pelz B, Ferrer JM, Kim T, Lang MJ, Kamm RD. 2009 Cytoskeletal deformation at high strains and the role of cross-link unfolding or unbinding. *Cell Mol Bioeng* **2**, 28–38.

23. Müller KW, Cyron CJ, Wall WA. 2015 Computational analysis of morphologies and phase

transitions of cross-linked, semi-flexible polymer networks. *Proc R Soc Lond A Math Phys Sci* **471**, 20150332.

24. Müller KW, Birzle AM, Wall WA. 2016 Beam finite-element model of a molecular motor for the simulation of active fibre networks. *Proc R Soc Lond A Math Phys Sci* **472**, 20150555.

25. Kim MC, Silberberg YR, Abeyaratne R, Kamm RD, Asada HH. 2018 Computational modeling of three-dimensional ECM-rigidity sensing to guide directed cell migration. *Proc Natl Acad Sci U S A* **115**, E390–E399.

26. Head D, Levine A, MacKintosh F. 2003 Distinct regimes of elastic response and deformation modes of cross-linked cytoskeletal and semiflexible polymer networks. *Phys Rev E* **68**, 061907.

27. Head D, Levine A, MacKintosh F. 2005 Mechanical response of semiflexible networks to localized perturbations. *Phys Rev E* **72**, 061914.

28. Han YL, Ronceray P, Xu G, Malandrino A, Kamm RD, Lenz M, Broedersz CP, Guo M. 2018 Cell contraction induces long-ranged stress stiffening in the extracellular matrix. *Proceedings of the National Academy of Sciences* **115**, 4075–4080.

29. Berthier E, Yang H, Guo M, Ronceray P, Broedersz CP. 2022 Nonlinear mechanosensation in fiber networks. *arXiv preprint arXiv:2208.06328*.

30. Unterberger MJ, Holzapfel GA. 2014 Advances in the mechanical modeling of filamentous actin and its cross-linked networks on multiple scales. *Biomech Model Mechanobiol* **13**, 1155–1174.

31. Flory PJ, Rehner Jr J. 1943 Statistical mechanics of cross-linked polymer networks I. Rubberlike elasticity. *J Chem Phys* **11**, 512–520.

32. Wang MC, Guth E. 1952 Statistical theory of networks of non-Gaussian flexible chains. *J Chem Phys* **20**, 1144–1157.

33. Arruda EM, Boyce MC. 1993 A three-dimensional constitutive model for the large stretch behavior of rubber elastic materials. *J Mech Phys Solids* **41**, 389–412.

34. Treloar L, Riding G. 1979 A non-Gaussian theory for rubber in biaxial strain. I. Mechanical properties. *Proc R Soc Lond A Math Phys Sci* **369**, 261–280.

35. Miehe C, Göktepe S, Lulei F. 2004 A micro-macro approach to rubber-like materials—part I: the non-affine micro-sphere model of rubber elasticity. *J Mech Phys Solids* **52**, 2617–2660.

36. Unterberger MJ, Schmoller KM, Bausch AR, Holzapfel GA. 2013a A new approach to model cross-linked actin networks: multi-scale continuum formulation and computational analysis. *J Mech Behav Biomed Mater* **22**, 95–114.

37. Unterberger MJ, Schmoller KM, Wurm C, Bausch AR, Holzapfel GA. 2013b Viscoelasticity of cross-linked actin networks: Experimental tests, mechanical modeling and finite-element analysis. *Acta Biomater* **9**, 7343–7353.

38. Holzapfel GA, Unterberger MJ, Ogden RW. 2014 An affine continuum mechanical model for cross-linked F-actin networks with compliant linker proteins. *J Mech Behav Biomed Mater* **38**, 78–90.

39. Storm C, Pastore JJ, MacKintosh FC, Lubensky TC, Janmey PA. 2005 Nonlinear elasticity in biological gels. *Nature* **435**, 191–194.

40. Broedersz C, Storm C, MacKintosh F. 2008 Nonlinear elasticity of composite networks of stiff biopolymers with flexible linkers. *Phys Rev Lett* **101**, 118103.

41. Broedersz CP, Mao X, Lubensky TC, MacKintosh FC. 2011 Criticality and isostaticity in fibre networks. *Nat Phys* **7**, 983–988.

42. Broedersz C, Sheinman M, MacKintosh F. 2012 Filament-length-controlled elasticity in 3D fiber networks. *Phys Rev Lett* **108**, 078102.

43. Chandran PL, Barocas VH. 2006 Affine versus non-affine fibril kinematics in collagen networks: theoretical studies of network behavior. *J Biomech Eng*.

44. Stracuzzi A, Britt BR, Mazza E, Ehret AE. 2022 Risky interpretations across the length scales: continuum vs. discrete models for soft tissue mechanobiology. *Biomech Model Mechanobiol* **21**, 433–454.

45. Mogilner A, Edelstein-Keshet L. 2002 Regulation of actin dynamics in rapidly moving cells: a quantitative analysis. *Biophys J* **83**, 1237–1258.

46. Othmer H. 2019 Eukaryotic cell dynamics from crawlers to swimmers. *Wiley Interdiscip Rev Comput Mol Sci* **9**, e1376.

47. Haspinger DC, Klinge S, Holzapfel GA. 2021 Numerical analysis of the impact of cytoskeletal actin filament density alterations onto the diffusive vesicle-mediated cell transport. *PLoS Comput Biol* **17**, e1008784.

48. Oelz DB. 2021 Quasi-steady-state reduction of a model for cytoplasmic transport of secretory vesicles in stimulated chromaffin cells. *J Math Biol* **82**, 1–25.

49. Wang N, Tolic-Nørrelykke IM, Chen J, Mijailovich SM, Butler JP, Fredberg JJ, Stamenovic D. 2002 Cell prestress. I. Stiffness and prestress are closely associated in adherent contractile cells. *Am J Physiol Cell Physiol* **282**, C606–C616.

50. Stamenovic D, Suki B, Fabry B, Wang N, Fredberg JJ, Buy JE. 2004 Rheology of airway smooth muscle cells is associated with cytoskeletal contractile stress. *J Appl Physiol* **96**, 1600–1605.

51. Coughlin MF, Stamenović D. 2003 A prestressed cable network model of the adherent cell cytoskeleton. *Biophys J* **84**, 1328–1336.

52. Blundell J, Terentjev E. 2009 Stretching semiflexible filaments and their networks. *Macromolecules* **42**, 5388–5394.

53. Heussinger C, Schaefer B, Frey E. 2007 Nonaffine rubber elasticity for stiff polymer networks. *Phys Rev E* **76**, 031906.

54. Blundell JR, Terentjev EM. 2011 The influence of disorder on deformations in semiflexible networks. *Proc R Soc Lond A Math Phys Sci* **467**, 2330–2349.

55. Broedersz C, MacKintosh F. 2011 Molecular motors stiffen non-affine semiflexible polymer networks. *Soft Matter* **7**, 3186–3191.

56. Barry RG, Hill NA, Stewart PS. 2022 Continuum soft tissue models from upscaling of arrays of hyperelastic cells. *Proc R Soc Lond A Math Phys Sci* **478**, 20220065.

57. Spencer AJM. 2014 *Continuum theory of the mechanics of fibre-reinforced composites* vol. 282. Springer.

58. Logg A, Mardal KA, Wells G. 2012 *Automated solution of differential equations by the finite element method: The FEniCS book* vol. 84. Springer Science & Business Media.

59. Lieleg O, Schmoller K, Claessens MMAE, Bausch AR. 2009 Cytoskeletal polymer networks: viscoelastic properties are determined by the microscopic interaction potential of cross-links. *Biophys J* **96**, 4725–4732.

60. Lieleg O, Claessens MM, Bausch AR. 2010 Structure and dynamics of cross-linked actin networks. *Soft Matter* **6**, 218–225.

61. Van Oosterwyck H, Rodríguez JF, Doblaré M, García Aznar JM. 2013 An affine micro-sphere-based constitutive model, accounting for junctional sliding, can capture F-actin network mechanics. *Comput Methods Biomech Biomed Engin* **16**, 1002–1012.

62. Thekkethil N, Jakub K, Guo M, Stewart PS, Hill NA, Luo X et al.. 2023 Multiscale Modelling of the Poroviscoelastic Rheology of Cell Cytoplasm. *Research Square Preprint, doi: https://doi.org/10.21203/rs.3.rs-3687649/v1*.

63. Preziosi L, Scianna M. 2016 Mathematical models of the interaction of cells and cell aggregates with the extracellular matrix. In *Mathematical models and methods for living systems* pp. 131–210. Springer.

64. Tsingos E, Bakker BH, Keijzer KA, Hupkes HJ, Merks RM. 2023 Hybrid cellular Potts and bead-spring modeling of cells in fibrous extracellular matrix. *Biophysical Journal*.